

Measurement of the optical extinction coefficients of post-flame soot in the infrared

J.F. Widmann*, J.C. Yang, T.J. Smith, S.L. Manzello, G.W. Mulholland

National Institute of Standards and Technology (NIST), 100 Bureau Drive, Gaithersburg, MD

Received 31 October 2002; received in revised form 20 February 2003; accepted 27 March 2003

Abstract

The optical extinction coefficients of post-flame soot have been measured in the wavelength range 2.8 to 4.1 μm . A laminar diffusion burner was combined with an infrared spectrograph and gravimetric measurements to determine the mass specific extinction coefficient, σ_s , and the dimensionless extinction coefficient, K_e . Using ethene gas as the fuel, the burner was operated at four global equivalence ratios ($\phi = 0.8, 1.0, 2.0,$ and 3.0) to examine the effect of the fuel-air ratio on the extinction coefficient. The extinction coefficient was found to decrease with increasing values of the global equivalence ratio for $\phi = 1.0, 2.0,$ and 3.0 . The results for $\phi = 0.8$ and $\phi = 1.0$ were in agreement to within the uncertainty of the measurements. Measurements were obtained using propane gas as the fuel ($\phi = 1.0$) and resulted in extinction coefficients equivalent to those of ethene. Transmission electron microscopy (TEM) images revealed differences in the morphology of the particles, consistent with the quantitative differences observed in the extinction data. The data indicate that the equivalence ratio has a strong effect on the optical properties of post-flame soot agglomerates. © 2003 The Combustion Institute. All rights reserved.

Keywords: Soot; Extinction coefficient; Radiation; Smoke

1. Introduction

Accurate determination of the optical properties of soot aerosol is essential for the interpretation of laser-based diagnostic measurements and the prediction of radiation transport through smoke. For example, the Fire Dynamics Simulator (FDS) developed at the National Institute of Standards and Technology (NIST) is used to predict large-scale fire phenomena [1,2] in a wide variety of fire scenarios. However, to include the effect of radiation transport through smoke-filled enclosures on the fire dynamics, it is

necessary to provide optical characteristics of the soot aerosol. Numerous studies of the optical extinction coefficients of soot particles in the visible and near-infrared regions of the electro-magnetic spectrum have been conducted [3–9]; however, such measurements have not been obtained in the mid-infrared. Radiative heat transfer within fires is dominated by radiation transport over the wavelength range from 2 to 5 μm , and thus, accurate measurements of soot optical properties in this range are essential to obtain accurate predictions from fire dynamics models.

The transmission, T , of radiation through an aerosol dispersion (neglecting absorption due to the continuous phase) can be quantified using the expression

$$T = \frac{I}{I_0} = \exp(-\sigma_s m_s L) = \exp\left(-K_e \frac{f_v}{\lambda} L\right), \quad (1)$$

* Corresponding author. Tel.: 603-643-2600; fax: 603-643-3967.

Currently at: Fluent Inc., 10 Cavendish Court, Lebanon, NH 03766.

E-mail address: jfw@fluent.com (J.F. Widmann).

where I_0 and I correspond to the incident and transmitted radiant intensities, respectively. Here, σ_s is the mass specific extinction coefficient, m_s is the mass of aerosol per unit volume, and L is the path length. In general, σ_s may be a function of the radiation wavelength, λ , and the aerosol properties (chemical composition, temperature, morphology, and size distribution). Application of Eq. 1 requires that the aerosol dispersion be homogeneous along the path length. Accurate knowledge of σ_s permits measurement of m_s using non-intrusive laser-extinction techniques, provided the particle size dependence of σ_s is neglected and the aerosol dispersion is assumed homogeneous. Reliable values for σ_s are also necessary to include the effect of particles in radiation-transport calculations in fires and combustion systems. The second expression in Eq. 1 is expressed in terms of the soot volume-fraction, f_v , and the dimensionless extinction coefficient, K_e . The two extinction coefficients are related by

$$K_e = \sigma_s \lambda \rho_s \quad (2)$$

where ρ_s is the density of the condensed phase.

In theory, one can predict the mass specific extinction coefficient from knowledge of the soot refractive index and a suitable model of the scattering and absorption of radiation by the particles. However, this is complicated by very large uncertainties in the refractive index of soot particles and light-scattering models that have not yet been sufficiently validated [10–14]. Rayleigh theory [15] is frequently used to predict the extinction of visible and infrared radiation due to soot particles; however, significant uncertainties result from combining such a simple theory with measured optical constants containing large uncertainties themselves. For example, using Rayleigh theory with the values of the refractive index reported by Dalzell and Sarofim [10], the predicted values of the mass specific extinction coefficient, σ_s , for acetylene and propane at $\lambda = 0.649 \mu\text{m}$ are $3.2 \text{ m}^2 \text{ g}^{-1}$ ($K_e = 3.9$, assuming $\rho_s = 1.86 \text{ g m}^{-3}$) and $3.8 \text{ m}^2 \text{ g}^{-1}$ ($K_e = 4.6$), respectively. For comparison, Mulholland and Croarkin [16] reported that $\sigma_s = 8.7 \text{ m}^2 \text{ g}^{-1}$ was the best estimate of the mean value determined from a literature search of experimental measurements (various fuels) obtained at $\lambda = 0.633 \mu\text{m}$. This corresponds to a dimensionless extinction coefficient $K_e = 10.2$, assuming $\rho_s = 1.86 \text{ g m}^{-3}$, which is more than twice the predicted values. As such, direct experimental measurement is currently a preferable approach to determining the optical extinction coefficient of post-flame soot.

This paper describes experimental measurements of σ_s for post-flame soot in the wavelength range 2.8 to 4.1 μm , which encompasses an important region

of the electromagnetic spectrum for radiant heat transfer in fires. The measured values of σ_s permit improved radiative transport calculations in enclosure fires, where thermal radiation through hot and cold smoke layers represents a significant fraction of the total energy budget. Furthermore, the effect of the global equivalence ratio is investigated because the concentration of oxygen in enclosures frequently varies with time.

2. Experimental apparatus

The experimental apparatus, presented in Fig. 1, consists of a flow-control system, a laminar diffusion burner, a black-body source, and an infrared spectrograph. The soot aerosol is generated in the burner, diluted with nitrogen (N_2), and carried by the combustion gases and N_2 to the optical cell. The apparatus is equipped with filters to remove particles from the gas stream before the measurement, or to measure gravimetrically the mass of soot aerosol present upstream and downstream of the optical cell. A sedimentation cell is also in-line to remove the largest soot agglomerates from the aerosol. The sedimentation cell is to reduce soot deposition in the optical cell and associated tubing. Soot deposition is an important issue because of the high particle concentrations required to perform extinction measurements at infrared wavelengths. Down-stream of the optical cell, the particles are filtered from the gas stream before the gas enters the pump. A mass flow controller is used to regulate the gas flow-rate through the optical cell.

The laminar diffusion burner consists of two concentric tubes, with fuel and air flowing through the inner and outer tubes, respectively. The data presented here correspond to experiments in which ethene and propane were used as the fuel. The inner diameters of the fuel and air tubes are 9 and 35 mm, respectively. The combustion products flow through a Pyrex¹ tube with an inner diameter of 26 mm that extends 27 cm down-stream of the fuel and air ducts. An outer Pyrex tube surrounds the 27-cm-long Pyrex tube, as shown in Fig. 1. This outer tube has an inner diameter of 50 mm and extends 61 cm down-stream of the fuel and air ducts. N_2 is added between the inner and outer Pyrex tubes to dilute the aerosol down-stream of the inner Pyrex tube (see Fig. 1). A tripper plate located 30 cm down-stream of the fuel and air ducts is used to instigate turbulent mixing to produce a more homogeneous aerosol dispersion [17]. Before the tripper plate, the flame is laminar and steady.

The combustion gases and N_2 diluent transport the particles to the optical cell, where the extinction

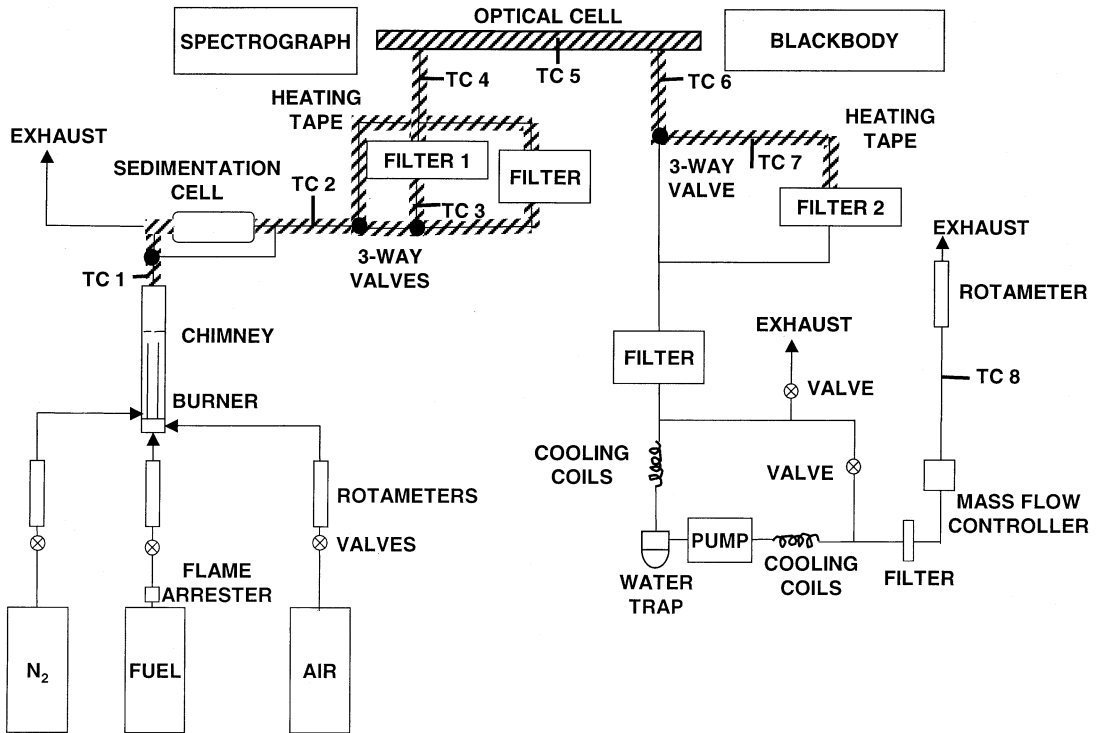


Fig. 1. Schematic of the experimental apparatus.

measurements are obtained. The Pyrex optical cell has a 25-mm inner diameter and a path length of $L = 38$ cm between the windows. Calcium fluoride (CaF_2) windows are used on the ends of the optical cell due to the superior transmission characteristics of CaF_2 in this wavelength range. The optical cell is wrapped with resistive heating tape, and the temperature is maintained at 50°C to prevent moisture condensation and minimize thermophoretic deposition of soot particles on the tube wall. The 50°C wall temperature was calculated to be well above the dew-point temperature for all operating conditions.

The extinction measurements are obtained by comparing the transmission of radiation through the optical cell with and without soot aerosol present. A black-body is used to provide radiation with a well-characterized distribution of spectral intensity. The intensity of the radiation is measured as a function of wavelength using a unique imaging spectrograph. The spectrograph contains a two-dimensional PtSi CCD array. The 320×244 element array is situated in a Stirling cooled package, and the temperature of the array is maintained at 77 K. A personal computer with an ITI frame-grabber board (12-bit resolution) was implemented to acquire and store the raw pixel voltages. The CCD array was combined with the necessary optics to obtain spectral information along

one axis of the two-dimensional array and spatial information along the other axis [18].

The spectral dimension of the CCD array was calibrated by positioning a narrow-band optical filter in front of the black-body aperture. The resulting image corresponds to a narrow band of high-intensity signal centered at the center wavelength of the filter. Using two narrow-band filters, a linear wavelength calibration was developed for each position row of the array. The center wavelengths of the narrow-band filters were determined to be 2.56 and $4.35 \mu\text{m}$ using an Fourier Transform Infrared (FTIR) spectrometer. For each of the filters, the location on the CCD array corresponding to the center wave-length (as determined from the midpoint of the peak width at the half-maximum height) was determined by linear interpolation. Thus, the wavelength calibration corresponds to sub-pixel accuracy.

The calibration of the signal intensity (pixel voltage to radiant intensity) was performed by imaging the aperture of the black-body at various temperatures and using Planck's law to relate the black-body temperature to a radiant intensity. A quadratic function was obtained relating the incident intensity to the pixel voltage at each pixel. Calibrations were performed using a Mikron black-body with a 50.8-mm aperture. Figure 2 presents the responsivity-vs.-

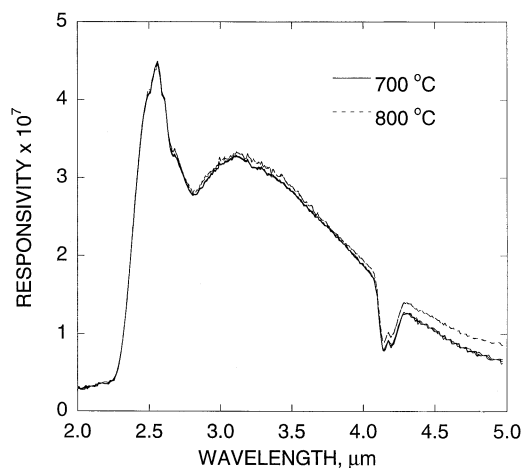


Fig. 2. Measured responsivity of the infrared spectrograph.

wave-length curve obtained from the calibrations. The responsivity is the ratio of the spectrograph signal to the radiant flux and shows the wavelength regions where the spectrograph is most sensitive. The data in Fig. 2 correspond to the 100th position row of the CCD array. Three replicated data sets are presented at each temperature, showing excellent repeatability. It should be noted, however, that the responsivity for the two different temperatures matched well below $4 \mu\text{m}$ but exhibited a disparity above $4 \mu\text{m}$. The disparity is likely due to the non-linearity of the calibration curves that results from the CCD array and the transmission characteristics of the optics. This issue is still being investigated, but it does not affect the data presented here, which were limited to $\lambda \leq 4.0 \mu\text{m}$. Note that the significant variation in the responsivity data presented in Fig. 2 indicates that the uncertainty in the data obtained with the spectrograph will be a function of wavelength. The dips in the responsivity curves near 2.7 and $4.2 \mu\text{m}$ are a result of absorption by ambient H_2O and CO_2 . To ensure that the calibration procedure was performed correctly, a black-body aperture was imaged with the spectrograph, and the temperature was determined by fitting Planck's spectral-distribution curve to the measured intensities with respect to wavelength. The results, reported elsewhere [19], indicate that the calibration was performed correctly.

The calculation of the mass specific extinction coefficient, σ_s , requires the determination of the concentration on a mass basis of the aerosol dispersion, m_s , as shown in Eq. 1. The mass concentration of particles in the optical cell is determined gravimetrically by alternately collecting the soot on membrane filters up-stream and down-stream of the optical cell.

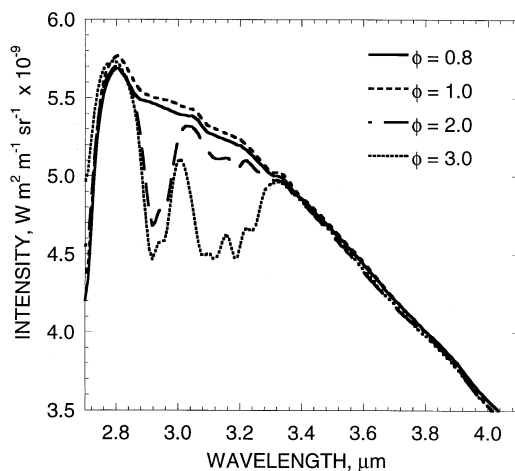


Fig. 3. Measured radiant intensity through combustion gases in the absence of soot particles. Ethene is the fuel.

The filters used for the gravimetric measurements are labeled filter 1 and filter 2 in Fig. 1. Additional details of the apparatus and calibration procedures are available elsewhere [19].

The primary particle sizes of the soot agglomerates were evaluated using transmission electron microscopy (TEM). Soot agglomerates were sampled from within the optical cell using a holder designed to accommodate copper TEM grids (3 mm in diameter, 200-mesh with carbon substrate). The sampled soot agglomerates were imaged using a Phillips EM400T TEM operated at 46 K. The micrographs obtained from the TEM analysis were placed on a light table and imaged using a CCD camera fitted with an 18- to 108-mm lens. The attached 18- to 108-mm zoom lens provided further magnification of the image required for primary particle measurements. The images were digitized using a frame-grabber board at 800×600 pixel resolution. Spatial calibration was obtained using separate TEM grids deposited with $100 \pm 3 \text{ nm}^2$ polystyrene latex spheres. The primary particles were measured using an edge-identification technique [20].

3. Results and discussion

Figure 3 presents the measured intensity transmitted through the optical cell when combustion gases are present but the soot has been filtered from the gas stream before entering the cell. The measured spectra for global equivalence ratios (the fuel-air ratio divided by the fuel-air ratio under stoichiometric conditions) of $\phi = 0.8$ and $\phi = 1.0$ show good agreement; however, the spectra for $\phi = 2.0$ and $\phi = 3.0$

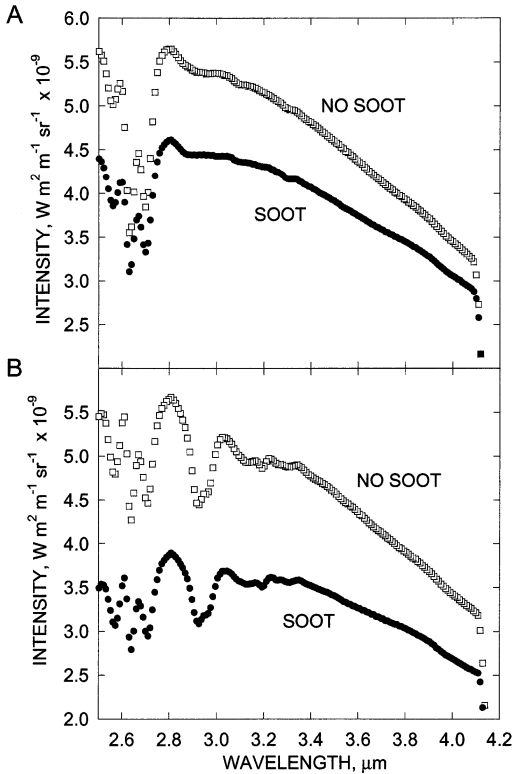


Fig. 4. Measured intensity with and without soot present for global equivalence ratios of (A) $\phi = 1.0$ and (B) $\phi = 2.0$.

show decreases in intensity near $\lambda = 2.9$ and $3.1 \mu\text{m}$. Note that the global equivalence ratio was varied by varying the air flow-rate while maintaining the fuel flow-rate at $6.2 \text{ cm}^3 \text{ s}^{-1}$. The decrease in intensity in these regions for the under-ventilated cases ($\phi > 1$) is due to absorption of gas-phase ethene. Gas-phase absorption has the potential to increase the uncertainty in the measurements in these regions if the concentration of unburned fuel differs for the measurements with and without soot. However, it will be shown that this effect is removed when the intensity curves measured with soot present are divided by the intensity curves obtained without soot, and that the data are reliable in these wavelength regions.

To determine the extinction coefficient of the soot aerosol, the intensity of radiation reaching the CCD detector from the black-body is measured with and without aerosol present in the optical cell. Figure 4 presents representative measurements of radiant intensity as a function of wavelength for two values of the global equivalence ratio, ϕ , when soot is and is not present. The black-body was set at a nominal temperature of 900°C , which provided sufficient intensity for the measurements without saturating the CCD array when soot was not present. The data in

Fig. 4 correspond to the mean measured intensity from ~ 50 to 60 position rows in the center of the aperture image, which corresponds to the length of the black-body aperture that could be imaged through the optical cell. The ratio of the two curves in Fig. 4 labeled “SOOT” and “NO SOOT” can be used to calculate the transmission, T , in Eq. 1. Note that the reliability of the data is compromised in regions of strong, ambient gas absorption (e.g., $4.1\text{--}4.4 \mu\text{m}$ due to CO_2), but not in the region of absorption due to unburned fuel. Also, as noted previously, the responsivity of the spectrograph is low below $2.5 \mu\text{m}$, which is evident from Fig. 2, and thus, this portion of the spectra is not shown in the figure. The data reported below correspond to the wave-length range $2.8\text{--}4.1 \mu\text{m}$, which corresponds to the region where the spectrograph provides accurate data free of interference from gas absorption bands.

The data presented here correspond to steady-state experiments in which spectra are obtained when soot is either flowing through, or being filtered before, the optical cell. However, one possible, time-varying aspect of the experiment deserves additional attention. If soot deposits on the windows of the optical cell during the experiment, the measured intensity will decrease with time. This was observed initially and was overcome by measuring the intensity as a function of time and extrapolating back to time zero (the time that soot was first introduced into the optical cell). This extrapolation was possible because the spectrograph obtains the entire spectra essentially instantaneously as opposed to a monochromator that must scan through the wavelength range of interest. It is believed that the noticeable decrease in signal was due to deposition of the large soot agglomerates on the optical windows. When the sedimentation cell shown in Fig. 1 was installed, the larger agglomerates were removed before entering the optical cell, and the measured intensity was much more steady over time. Figure 5 presents the normalized intensity measured at $3.47 \mu\text{m}$ for three representative experiments ($\phi = 1.0$) in which the sedimentation cell was used. The data show that the intensity does not decrease significantly during the experiment. The data presented for $t < 0$ corresponds to measurements obtained before the soot was introduced into the optical cell.

It is recognized that inclusion of the sedimentation cell may introduce a biasing in the measured values of the mass specific extinction coefficient due to modification of the soot aerosol-size distribution. This is because the extinction coefficient is composed of two parts, scattering and absorption. It is known that particle size will have a strong effect on radiation scattering, while it is generally accepted that radiant absorption will depend much more weakly upon the

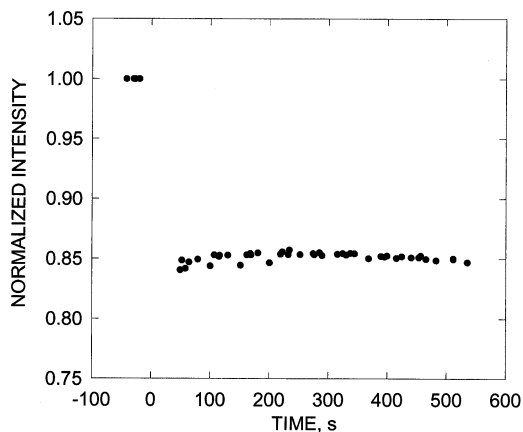


Fig. 5. Normalized intensity as a function of time ($\lambda = 3.47 \mu\text{m}$).

particle size. Mulholland and Choi [6] measured the scattering albedo of soot aerosol produced by laminar ethene flames in the visible region ($\lambda = 632.8 \text{ nm}$) and found the scattering component represented $\sim 19\%$ of the total extinction. The wave-lengths reported here are approximately 4.5–6.5 times greater than the visible wavelength used in that study. Thus, the scattering component is expected to be less significant for infrared wavelengths than visible wavelengths, and the extinction coefficients measured here are expected to be approximately equal to the absorption coefficients.

Figure 6 presents the experimentally-determined values of the mass specific extinction coefficient, σ_s , as a function of wavelength for four values of the

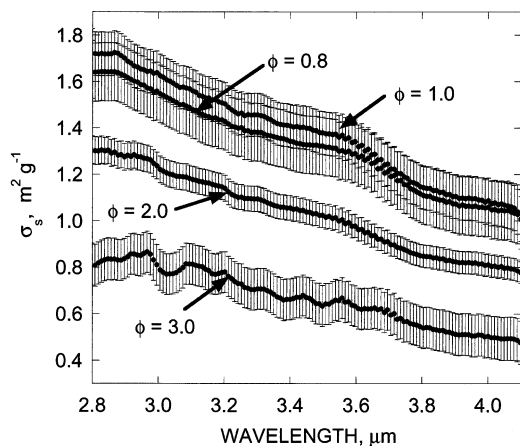


Fig. 6. Calculated values of the mass specific extinction coefficient, σ_s , for ethene and four values of the global equivalence ratio, ϕ .

global equivalence ratio. The extinction coefficients were calculated from Eq. 1, with the ratio I/I_0 obtained from the data in Fig. 4 and m_s determined from the gravimetric measurements. Note the strong dependence of σ_s on the equivalence ratio, ϕ . The data were obtained using ethene as the fuel, and the error bars correspond to the combined standard uncertainty [21,22]. Although the data presented in Fig. 6 suggest that stoichiometric conditions yield the maximum extinction, the difference in σ_s for $\phi = 1.0$ and $\phi = 0.8$ are within the experimental uncertainty. Thus, it can only be concluded that σ_s decreases with increasing ϕ for the under-ventilated cases. The uncertainty estimates were obtained from considerations of the uncertainty in the extinction measurements and the gravimetric measurements (which are independent), the components of which are summarized in the Appendix. For brevity, only the uncertainty budgets for $\phi = 1.0$ are presented. Because the extinction measurements are independent of the gravimetric measurements, the uncertainty of the wave-length dependence of the extinction coefficients is less than that suggested by the error bars in Fig. 6. For example, 75% of the uncertainty estimate corresponding to the extinction coefficients for $\phi = 1.0$ is composed of components from the gravimetric measurements (see Tables A1 and A2). Note that the data in Fig. 6 indicate that σ_s for $\phi = 1.0$ and $\lambda = 3.5 \mu\text{m}$ is $\sim 1.4 \text{ m}^2 \text{ g}^{-1}$. This is significantly higher than values obtained from Rayleigh theory. For example, the predicted values using Rayleigh theory with the refractive index values of Dalzell and Sarofim [10] and Felske et al. [12] are 0.78 and $0.47 \text{ m}^2 \text{ g}^{-1}$, respectively.

Figure 7 presents TEM images of soot agglomerates for four operating conditions. The four operating conditions correspond to ethene fuel burning under three values of the global equivalence ratio, ϕ , and propane fuel for one value of ϕ . The optical properties of the propane-generated soot are discussed below. The TEM images reveal an interesting feature of the morphology as the equivalence ratio is varied. For both fuels, the spheroidal primary particles are clearly noticeable for $\phi = 1$. However, when the equivalence ratio is increased, the primary particles become less apparent. The soot agglomerates generated in under-ventilated conditions have structures in which the primary particles are difficult to identify. The agglomerates have the appearance of either an adsorbed liquid phase or having the primary particles “fused” together. The effect also increases with increasing equivalence ratio. The qualitative differences in the TEM images are consistent with the quantitative differences in the optical properties of the soot with different values of ϕ .

The strong dependence of the measured extinction

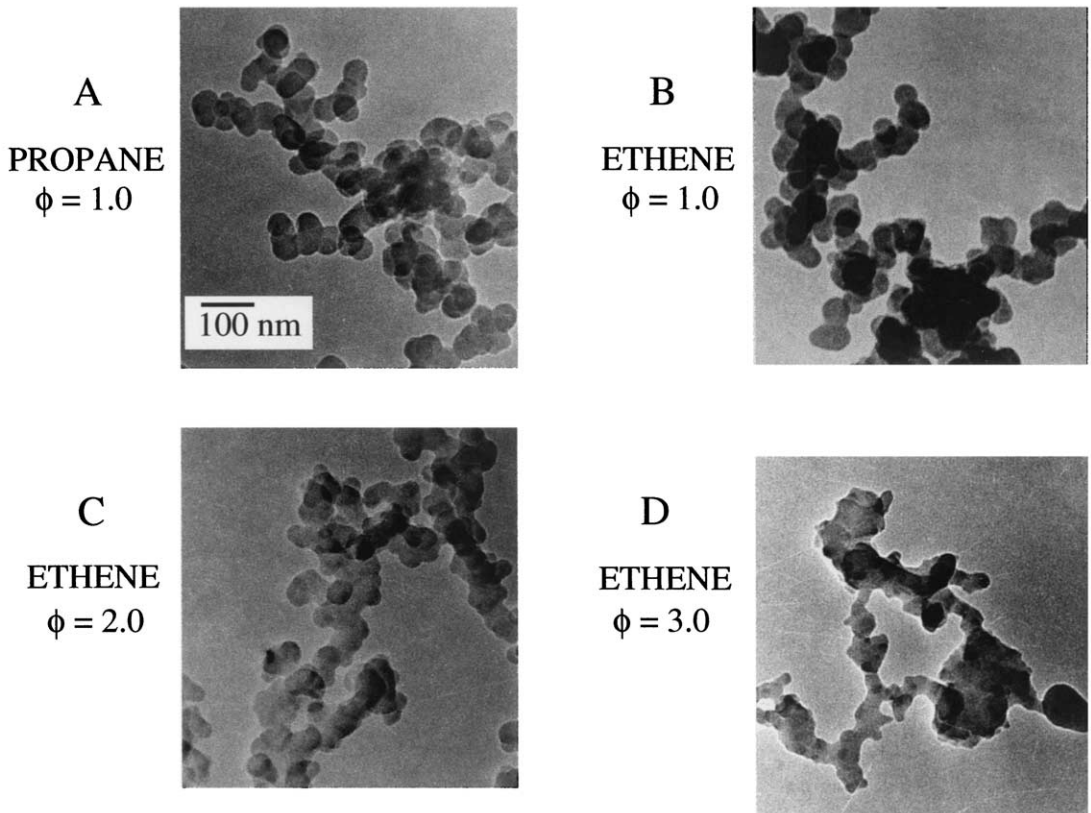


Fig. 7. TEM images of soot agglomerates produced in ethene and propane diffusion flames. The global equivalence ratio, ϕ , is given in the figure.

coefficient upon the equivalence ratio and the qualitative differences in the TEM images are likely related to the differences in the ratio of organic to elemental carbon in the soot particles. It is reasonable that under-ventilated combustion would result in soot particles containing higher concentrations of organic carbon due to the incomplete combustion. The increased organic content will result in differences in the refractive index when compared to soot particles with higher elemental carbon content. Differences in the imaginary component of the refractive index would be consistent with the strong dependence of the extinction coefficient with ϕ . Furthermore, a higher organic carbon concentration would likely correspond to soot particles with a lower melting point/range, which could result in the fusing of particles observed in the TEM images of soot produced at higher equivalence ratios. Because the measurements correspond to post-flame soot agglomerates, it is not possible to differentiate between organic carbon that may have been involved in the high-temperature soot formation process and that which condenses upon the particles in the post-flame region as

the gases cool. Fortunately, it is not necessary to make this distinction to apply the measured extinction coefficients to the calculation of radiation transport in fire scenarios.

Leonard et al. [17] measured the ratio of organic to elemental carbon in soot produced in a laminar, ethene diffusion flame and found a strong correlation with the global equivalence ratio. Their burner was very similar to the one used here, although the dimensions of the two concentric tubes were not identical. Nonetheless, the composition of the soot generated is expected to follow the same trends. They reported that the ratio of organic to elemental carbon was 0.04, 0.05, 0.48, and 1.13 for equivalence ratios of 0.5, 1, 2, and 4, respectively. Thus, the differences in the ratio of organic carbon to elemental carbon in the soot particles are consistent with the observed trends in the extinction coefficients and the TEM images. Furthermore, the agreement between the measured values of σ_s for $\phi = 0.8$ and $\phi = 1.0$ is consistent with the relatively constant values of the organic/elemental carbon ratios reported by Leonard et al. for these equivalence ratios.

Table 1
Gravimetric measurements of soot concentration (mg s^{-1})

Fuel	Equivalence Ratio, ϕ	Filter 1			Filter 2			Average	
		Mean, mg s^{-1}	Standard deviation, s_A	Number of samples, N	Mean, mg s^{-1}	Standard deviation, s_B	Number of samples, N	Mean, mg s^{-1}	Standard deviation, s^*
Ethene	0.8	0.0195	0.00275	16	0.0155	0.00149	16	0.0175	0.00156
Ethene	1.0	0.0208	0.00208	14	0.0153	0.00073	16	0.0181	0.00110
Ethene	2.0	0.0429	0.00201	13	0.0351	0.00114	14	0.0390	0.00115
Ethene	3.0	0.0168	0.00282	12	0.0131	0.00258	10	0.0150	0.00191
Propane	1.0	0.0321	0.00171	18	0.0258	0.00142	23	0.0290	0.00111

$$* s^2 = (0.5)^2 s_A^2 + (0.5)^2 s_B^2$$

As noted above, the measured extinction must be normalized by the mass concentration of aerosol present to obtain the mass specific extinction coefficient. The quantity of soot collected on the up-stream and down-stream filters is summarized in Table 1. The average value of the soot concentrations determined from the two filter measurements represents the best estimate of the true mass concentration in the optical cell, and this was used in the calculation of the extinction coefficients. On average, the gravimetric measurements obtained from filters 1 and 2 differed by $\sim 25\%$ of the mean; however, the uncertainty in the mean value is best estimated by the expression $\mu = (m_2 - m_1)/(2\sqrt{3})$, where m_1 and m_2 are the entering and exiting mass concentrations, respectively [21,22].

An implicit assumption in the use of Eq. 1 is that the aerosol is homogeneous along the path length. However, as shown in Table 1, the mass concentration exiting the optical cell is less than that entering the cell due to soot sedimentation within the cell. It is worth-while at this point to consider the effect of the non-uniform mass concentration on the measurement results. As mentioned, the decrease in mass concentration from filter 1 to filter 2 is due to sedimentation of soot particles within the optical cell. The cross-sectional area of the optical cell is considerably larger than the tubing leading to and from the optical cell; thus, the gas velocity is reduced significantly upon entering the cell, resulting in increased deposition. This is consistent with the observation that the quantity of soot obtained when the tubes are flushed with a high flow of N_2 gas is small compared to the quantity of soot obtained from within the optical cell. By making an assumption as to how the concentration varies along the length of the optical cell, x , and integrating the differential form of Eq. 1 from the entrance to the exit of the cell, the effect of the non-uniform soot concentration on the calculated extinction coefficients can be evaluated. Here, we use a lumped-parameter model in which variations are in

the x -direction only, and consider two forms of the concentration profile: linear and exponential.

A linear profile results from assuming that the sedimentation rate is constant along the length of the cell (zero-order loss rate), as given by

$$m(x) = m_1 + (m_2 - m_1)/(x/L). \quad (3)$$

Integration of the differential form of Eq. 1 using Eq. 3 for the mass concentration with respect to the path length yields Eq. 1, with $m_s = (m_2 + m_1)/2$. Thus, a linear-concentration profile within the optical cell results in the extinction being identical to that of a uniform-concentration profile equal to $(m_2 + m_1)/2$.

The exponential profile results if the rate of soot sedimentation within the optical cell is proportional to the concentration of soot in the gas phase (first-order loss rate). In this case, the mass concentration profile along the path length is

$$m(x) = m_1(m_2/m_1)^{x/L}. \quad (4)$$

Comparison of Eq. 3 and Eq. 4 reveals that the zero- and first-order-loss models result in concentration profiles that agree closely with a mean relative difference of only 0.5%. Thus, both models of loss within the optical cell are consistent with Eq. 1, with the mass concentration within the cell calculated from the mean of the entering and exiting particle concentrations.

Figure 8 presents the dimensionless extinction coefficient, K_e , calculated from Eq. 2. A value of $\rho_s = 1.86 \text{ g cm}^{-3}$ was assumed for the density of the condensed phase [3]. It is recognized that the density may also be a function of the elemental/organic carbon ratio; however, these data are not available, and thus, a frequently-used value for the condensed-phase soot density was used here. The dimensionless extinction coefficients show a slight decrease with increasing wavelength. Interestingly, there appears to be a broad peak in the extinction near $3.5 \mu\text{m}$. Due to measurement uncertainty, it is not known if this small peak is an instrument artifact or the result of absorp-

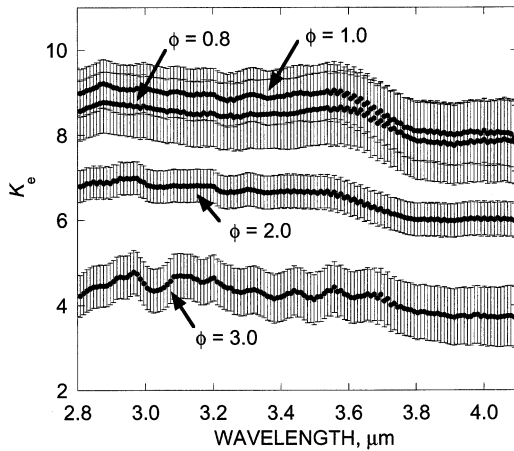


Fig. 8. Calculated values of the dimensionless extinction coefficient, K_e , for ethene and four values of the global equivalence ratio, ϕ .

tion due to C-H bonds. However, we note that the data presented in Fig. 3 corresponding to the measured intensity without soot do not reveal an increase in signal intensity over this wavelength range.

Although previously published data at these wave-lengths are unavailable, the data for $\phi = 1.0$ in Fig. 8 can be compared to measurements obtained at visible and near-infrared wavelengths. Mulholland and Choi [6] measured both the mass specific extinction coefficient σ_s and the scattering albedo ω of soot produced during combustion of ethene. They reported values of $8.5 \text{ m}^2 \text{ g}^{-1}$ and 0.186 for σ_s and ω , respectively. Using $\rho_s = 1.86 \text{ g cm}^{-3}$ and $\lambda = 0.6328 \text{ }\mu\text{m}$, a value of $K_e = 10.0$ is obtained. This is higher than the values of K_e obtained here (~ 8.0 to 9.0 for $\phi = 1.0$). However, if the scattering albedo is considered, the data of Mulholland and Choi suggest that the dimensionless absorption coefficient for ethene soot is ~ 8.1 , which agrees favorably with the data presented in Fig. 8. Mulholland and Croarkin [16] reviewed the published values of the mass specific extinction coefficient at $\lambda = 0.6328 \text{ }\mu\text{m}$ and concluded that a value of $\sigma_s = 8.7 \pm 1.1 \text{ m}^2 \text{ g}^{-1}$ was consistent with the available measurements. This corresponds to a dimensionless extinction coefficient of $K_e = 10.2 \pm 1.3$. Again, if the enhanced scattering albedo at visible wavelengths is considered, the data obtained here at infrared wavelengths show good agreement with the previously published values at $\lambda = 0.6328 \text{ }\mu\text{m}$. It was also shown above that the measured values of σ_s and K_e are ~ 2 to 3 times larger than those obtained from applying Rayleigh theory with published values of the refractive index for soot [10,11].

Figure 9 presents comparisons of the mass spe-

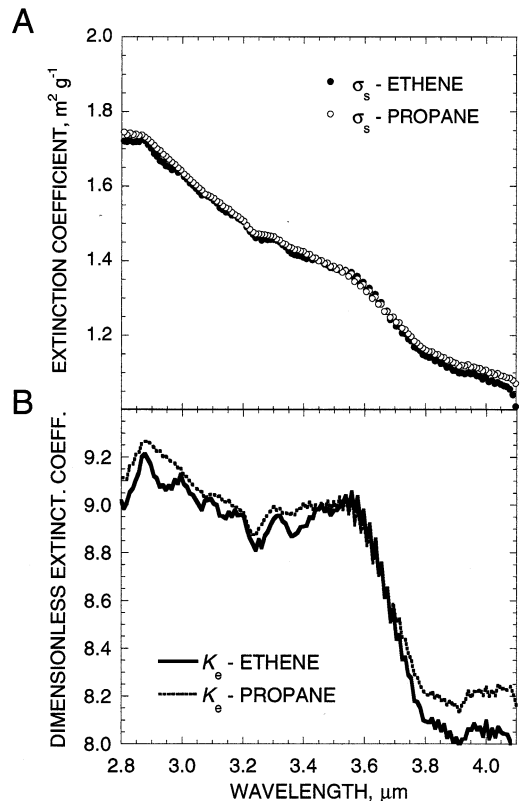


Fig. 9. Comparison of (A) the mass specific extinction coefficient, σ_s , and (B) the dimensionless extinction coefficient, K_e , for ethene and propane at a global equivalence ratio of $\phi = 1.0$.

cific extinction coefficients and dimensionless extinction coefficients for ethene and propane. The data for both fuels correspond to a global equivalence ratio of $\phi = 1.0$. The agreement between the extinction data for the two fuels is very good, indicating that there is a negligible effect of fuel source on the optical extinction for these two fuels. The peak in the extinction discussed above is evident in Fig. 9. The uncertainty estimates for the optical properties of the propane-generated soot are similar to those of the ethene-generated soot ($\phi = 1$). The primary particle sizes for propane ($\phi = 1$) and ethene ($\phi = 1$) were measured to be 48.1 nm , with a standard deviation of $s = 12.7 \text{ nm}$, and 45.1 nm with $s = 9.6 \text{ nm}$, respectively (based upon 200 primary particle-size measurements for each case). The measurement uncertainty in the mean primary particle size is estimated to be $\sim 3\text{--}4 \text{ nm}$. Thus, the mean primary particle sizes for the two fuels are equivalent to within the uncertainty in the measurement.

To some effect, the optical properties of soot particles may depend upon the C/H ratio of the fuel,

the temperature of the soot, and the extent of agglomeration. However, it has been reported that, in general, these effects are not significant (see Ref. [23], and the references cited therein). The data presented above, and those of Ref. [17], suggest that the air-fuel ratio may have a greater effect upon the optical properties and morphological structure of the soot agglomerates than any of these other factors. The data provide direct determination of the optical properties necessary to model radiation transport through smoke layers in enclosure fires, particularly the lower, cooler smoke layer. It is unknown if the higher temperatures in the upper layer will alter the properties of the post-flame soot agglomerates from those measured here. This issue is currently under investigation.

4. Conclusions

Mass specific extinction coefficients have been obtained for post-flame soot in the wavelength range 2.8–4.1 μm . To explore the effect of the global equivalence ratio on the optical extinction coefficients, ethene fuel was burned under conditions corresponding to $\phi = 0.8, 1.0, 2.0,$ and 3.0 . For the cases $\phi \geq 1$, the extinction coefficients were found to be a strong function of ϕ . The values of σ_s for $\phi = 0.8$ and $\phi = 1.0$ agreed to within the experimental uncertainty. Propane fuel was burned under conditions corresponding to $\phi = 1.0$ to compare with ethene fuel under the same global equivalence ratio, and this resulted in values of σ_s that agreed closely. The data indicate that the equivalence ratio is an important parameter in determining the optical extinction coefficients of the post-flame soot aerosol, but that the fuel source is not. The effects of the global equivalence ratio on the optical and morphological properties of the soot reported here are consistent with the strong effect of equivalence ratio on the organic/elemental carbon ratio reported by Leonard et al. [17]. The data indicate that accurate prediction of fire dynamics in environments in which radiative heat transfer is important will require inclusion of the effect of fuel-air ratio on the optical properties of the smoke.

Notes

1. Certain commercial equipment, instruments, or materials are identified in this paper to specify adequately the experimental procedure. Such identification does not imply recommendation or endorsement by the National Institute of Standards and Technology, nor does it imply that the materials or equipment are necessarily the best available for this purpose.

2. The expressed uncertainty corresponds to one standard deviation, s .

Acknowledgments

The authors would like to acknowledge the assistance of Marco Fernandez with the assembly of the experimental apparatus. The assistance of Masrifa Tasnim, a student intern in the authors' laboratory, is also gratefully acknowledged. One of the authors (S.L.M.) would like to acknowledge the financial support of the NIST/NRC Postdoctoral Research Program.

References

- [1] H.R. Baum, K.B. McGrattan, R.G. Rehm, J. Heat Transfer Soc. Jpn. 35 (1997) 45.
- [2] K.B. McGrattan, H.R. Baum, R.G. Rehm, Fire Safety J. 30 (1998) 161.
- [3] R.A. Dobbins, G.W. Mulholland, N.P. Bryner, Atmos. Environ. 28 (1994) 889.
- [4] M.Y. Choi, G.W. Mulholland, A. Hamins, T. Kashiwagi, Combust. Flame 102 (1995) 161.
- [5] I. Colbeck, B. Atkinson, Y. Johar, J. Aerosol Sci. 28 (1997) 715.
- [6] G.W. Mulholland, M.Y. Choi, Twenty-seventh Symposium (International) on Combustion, The Combustion Institute, 1998, p. 151.
- [7] J. Zhu, M.Y. Choi, G.W. Mulholland, Mulholland, L.A. Gritzo, Proc. Combust. Inst., 28, 2000 p. 439.
- [8] J. Zhu, M.Y. Choi, G.W. Mulholland, L.A. Gritzo, Int. J. Heat Mass Transfer 43 (2000) 3299.
- [9] J. Zhu, M.Y. Choi, G.W. Mulholland, S.L. Manzello, L.A. Gritzo, J. Antilla-Suo, Proc. Combust. Inst. (2002) in press.
- [10] W.H. Dalmaz, A.F. Sarofim, J. Heat Transfer 91 (1969) 100.
- [11] S.C. Lee, C.L. Tien, Eighteenth Symposium (International) on Combustion, The Combustion Institute, 1981, pp. 1159–1166.
- [12] J.D. Felske, T.T. Charalampopoulos, H.S. Hura, Combust. Sci. Technol. 37 (1984) 263.
- [13] Z.G. Habib, P. Vervisch, Combust. Sci. Technol. 59 (1988) 261.
- [14] T.T. Charalampopoulos, H. Chang, B. Stagg, Fuel 68 (1989) 1173.
- [15] H.C. van de Hulst, Light Scattering by Small Particles, General Publishing Company, Ltd., Toronto, Ontario, 1957.
- [16] G.W. Mulholland, C. Croarkin, Fire Mater. 24 (2000) 227.
- [17] S. Leonard, G.W. Mulholland, R. Puri, R.J. Santoro, Combust. Flame 98 (1994) 20.
- [18] Sivathanu, Y., Joseph, R., Lim, J., Zheng, Y., Gore, J. Rapid Scanning Infrared/Near Infrared Spectrometer: Phase 2 SBIR Final Report, NIST GCR 99-777, 1999.

- [19] J.F. Widmann, J.C. Yang, M. Bundy, B.K. Tsai, and G.W. Mulholland, *Rev. Sci. Instrum.* 74 (2003) 938.
- [20] S.L. Manzello, M.Y. Choi, *Int.J. Heat Mass Transfer* 45 (2002) 1109.
- [21] B.N. Taylor, C.E. Kuyatt, *Guidelines for Evaluating and Expressing the Uncertainty of NIST Measurement Results*. NIST Technical Note 1297, National Institute of Standards and Technology, Gaithersburg, MD, 1984.
- [22] American National Standard for Expressing Uncertainty, U.S. Guide to the Expression of Uncertainty in Measurement, ANSI/NCSL Report Z540-2-1997, National Conference of Standards Laboratories, 1997.
- [23] K.C. Smyth, C.R. Shaddix, *Combust. Flame* 107 (1996) 314.

Table A1
Uncertainty budget for the mass specific extinction coefficient, σ_s (Ethene, $\phi = 1$, $\lambda = 3.5 \mu\text{m}$)

Source of Uncertainty	Standard Uncertainty $\text{m}^2 \text{g}^{-1}$	
	Type A	Type B
Intensity ratio, I/I_0	0.022	
Wavelength, λ		0.014
Path length, L		0.0073
Mass concentration of soot, m_s		
Optical cell temperature		0.013
Soot losses in optical cell		0.0069
Filter weight	0.084	
Collection time		0.023
Gas flow rate		0.0069
Combined standard uncertainty ($k = 2$): $0.186 \text{ m}^2 \text{g}^{-1}$		

Table A2
Uncertainty budget for the dimensionless extinction coefficient, K_e (Ethene, $\phi = 1$, $\lambda = 3.5 \mu\text{m}$)

Source of Uncertainty	Standard Uncertainty $\text{m}^2 \text{g}^{-1}$	
	Type A	Type B
Mass specific extinction coefficient, σ_s		0.61
Condensed phase soot density, ρ_s		0.27
Wavelength, λ		0.090
Combined standard uncertainty ($k = 2$): 1.34		